Available online at www.sciencedirect.com
ScienceDirect
Trans. Nonferrous Met. Soc. China 31(2021) 3862−3878
Transactions of Nonferrous Metals Society of China
www.tnmsc.cn

Mechanical properties and rockburst proneness of phyllite under uniaxial compression

Xue-feng SI[1], Lin-qi HUANG[1], Xi-bing LI[1], Feng-qiang GONG[2], Xi-ling LIU[1]

1. School of Resources and Safety Engineering, Central South University, Changsha 410083, China;
2. School of Civil Engineering, Southeast University, Nanjing 211189, China

Received 18 December 2020; accepted 3 August 2021

Abstract: To investigate the influence of the bedding angle, β, on the mechanical properties and rockburst proneness, uniaxial compression tests were conducted using cylindrical phyllite specimens with different bedding angles. According to the results, the peak stress, peak strain, cumulative acoustic emission counts, and potential energy of the elastic strain exhibited a U-shaped change trend. With an increase in β from 0° to 90°, the failure mode transformed from tensile splitting failure along the bedding plane to shear slip failure along the weak bedding plane. Finally, the failure mode evolved into a tensile splitting failure across the bedding plane. When β=15°, 30°, and 45°, the phyllite specimens exhibited strong, slight, and moderate rockburst proneness, with strong, slight, and moderate shear slip rockbursts, respectively. When β=0°, 60°, 75°, and 90°, the phyllite specimens had extremely strong rockburst proneness, and an extremely strong strain rockburst occurred.

Key words: phyllite; bedding angle; mechanical properties; failure mode transformation; rockburst proneness

1 Introduction

Under complex geostress resulting from long geological evolution, rock masses, such as phyllites, shales, schists, and slates, form a bedding structure through sedimentation or metamorphism. Such a structure usually contains many discontinuous micro-defects. Phyllite is a typical fine-grained, microcrystalline, shallow metamorphic rock with a well-defined bedding structure. With a change in the bedding angle, bedding rock masses exhibit the characteristics of physical and mechanical anisotropy [1−5], which significantly influences underground engineering [6−8]. Many scholars have investigated the mechanical properties and failure criterion of bedding rocks (transversely isotropic rocks). HENG et al [9] and XU et al [10] determined the mechanical properties of bedding planes and the shear strength of shale with different bedding orientations under direct shear. They also studied the effect of bedding planes on the wave velocity and acoustic emission (AE) characteristics of shale for different coring directions under uniaxial compression. CHEN et al [11] conducted Brazilian tests to investigate the variation in the indirect tensile strength of sandstone with the inclination angle between the apparent rock layers and the applied diametric load. DUAN and KWOK [12] investigated the behaviors of anisotropic rocks in Brazilian tests based on discrete element method simulations, and they systematically studied the effect of weak layers on the indirect tensile strength, stiffness, and fracture patterns of the rocks. HOEK [13] established an empirical failure criterion based on a theoretical derivation; he discussed the advantages and limitations of this failure criterion and illustrated its application in practical geotechnical engineering design. SAROGLOU and TSIAMBAOS [14]

Corresponding author: Lin-qi HUANG, Tel: +86-13469059806, E-mail: huanglinqi@csu.edu.cn
DOI: 10.1016/S1003-6326(21)65770-9

reported that the Hoek–Brown criterion parameters were significantly influenced by the strength anisotropy of intact rock; they modified the criterion by incorporating a new parameter to account for the effect of strength anisotropy.

These previous studies investigated the mechanical properties of bedding rocks and determined the influence of bedding angles [15−17]. Phyllite, shale, and slate strata with obvious bedding structures, well-developed joints, and fissures are widely distributed in the mountainous areas of central and western China. Rockburst disasters often occur during tunnel engineering, mining, or hydropower station engineering in strata with bedding structures [18,19]. Most studies have focused on rock types with isotropic behavior (e.g., granites, sandstone, granodiorites, and diorites) [20−24]. However, few studies have focused on anisotropic rocks (e.g., phyllite, shale, and gneiss) [7], and the influence of the bedding angle on rockburst proneness has rarely been investigated.

In this study, to investigate the influence of the bedding angle on the mechanical properties and rockburst proneness, uniaxial compression tests were conducted using the INSTRON 1346 test system on *d*50 mm × 100 mm cylindrical phyllite specimens with different bedding angles. During the tests, the failure process was monitored and recorded using a high-speed camera, and the AE signals generated during the failure process were recorded using the AE system. The changes in the physical and mechanical properties of the phyllite specimens with different bedding angles were determined, relationships between the failure modes and the mechanical properties were analyzed, and rockburst proneness under different bedding angles was investigated. The influence of the bedding angle on the physical and mechanical properties, failure mode, rockburst proneness, and rockburst severity (rockburst grade) of the phyllite specimens was evaluated. The findings of this study can guide underground phyllite rock mass engineering.

2 Experimental

2.1 Specimen preparation

The phyllite material (see Fig. 1(a)) used in this study was obtained from Jiujiang City, Jiangxi Province, China. To determine its mineral composition, thin sections of the rock were analyzed using XRD. The mineral composition of the rock is approximately 27.56% quartz, 30.66% mica, 34.46% chlorite, and 7.32% feldspar, as shown in Fig. 1(b).

The bedding angle, β, is the angle between the axial stress σ_1 of the uniaxial compression test and the bedding plane, as shown in Fig. 2(a). The phyllite materials were processed into *d*50 mm × 100 mm cylindrical specimens with different values of β (0°, 15°, 30°, 45°, 60°, 75°, and 90°), as shown in Fig. 2(b). The machining precision strictly followed the standards of the International Society for Rock Mechanics. During specimen processing, the unevenness error of the two end surfaces was controlled within ±0.05 mm, and the deviation of the perpendicularity of the two end surfaces was controlled within ±0.25°.

2.2 Test system and experimental procedure

Before the test, the masses, sizes, and P-wave velocities of the phyllite specimens were measured

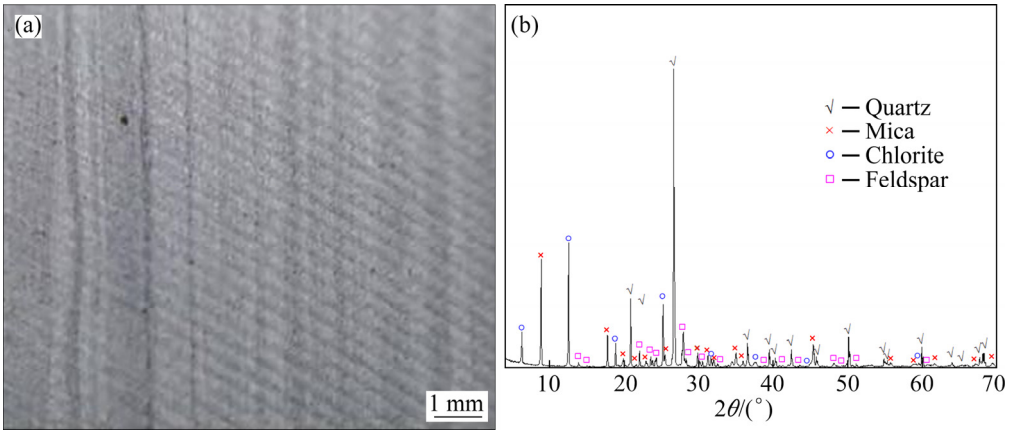

Fig. 1 Phyllite material: (a) Naked-eye observation; (b) XRD pattern

using an electronic scale (Fig. 3(a)), vernier caliper (Fig. 3(b)), and HS-YS4A rock acoustic wave parameter tester (Fig. 3(c)). Uniaxial compression tests were conducted using the INSTRON 1346 test system, as shown in Fig. 3(d). A high-speed camera was used to monitor and record the failure processes of the specimens. The resolution was set to 512×432, and the frame frequency of the high-speed camera was set to 125 frames per second (the time interval between two adjacent pictures was 8 ms). An AE system was used to collect the AE signals generated during the failure process, and two AE probes were arranged on the loading block of the INSTRON 1346 test bench (Fig. 3(d)). The sampling rate and threshold of the AE were 10 MHz and 40 dB, respectively. Two strain gauges were attached to the middle symmetrical position of the specimen to measure the axial and transverse deformations. During the tests, the axial loading rate was set to be 60 kN/min using load control. To prevent the impact of the testing machine when the specimen was damaged, which led to more serious damage of the specimen, the loading method was converted into displacement control when the axial stress was loaded to approximately 70 MPa (when the peak stress was low, the axial stress was loaded to approximately 40 MPa), and the loading rate was set to be 0.1 mm/min. To reduce the test error and increase the reliability of the test results, uniaxial compression tests of three phyllite specimens were conducted for each bedding angle, and the test results were the average values of the three specimens.

3 Experimental results

3.1 Characteristics of P-wave velocity of phyllite

The relationship between the P-wave velocity (v_p) and β of the phyllite specimens is illustrated in Fig. 4. As shown, v_p gradually decreases with increasing β. When β increased from 0° to 90°, the average v_p decreased from 6190 to 4529 m/s, a decrease of 1661 m/s (26.8% of the average v_p at β=0°). These results indicate that β significantly influences v_p. The mechanism of this influence is explained as follows.

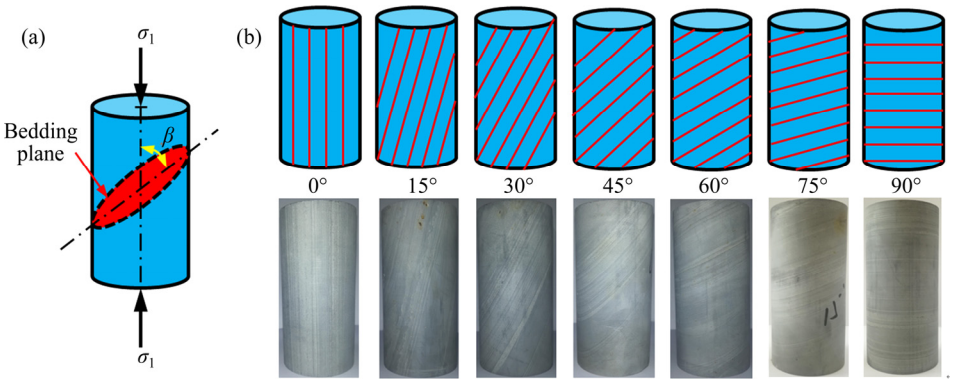

Fig. 2 Phyllite specimens: (a) Schematic of bedding angle; (b) Phyllite specimens with different bedding angles

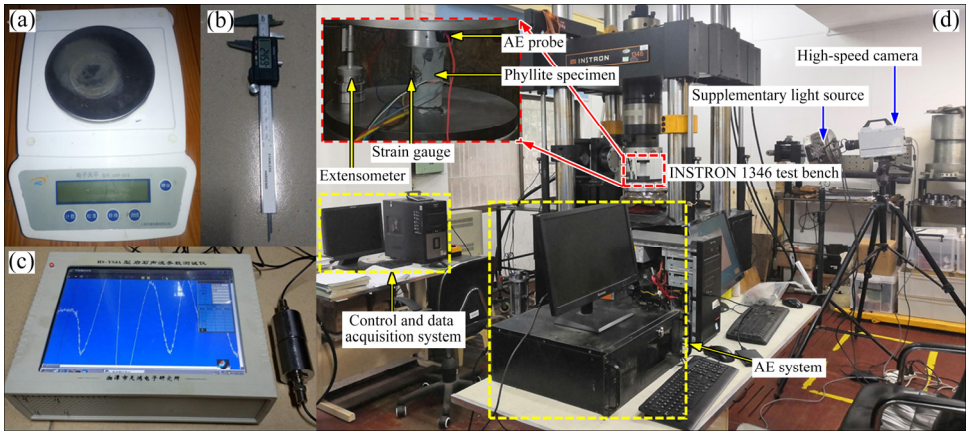

Fig. 3 Experiment apparatus: (a) Electronic scale; (b) Vernier caliper; (c) HS-YS4A rock acoustic wave parameter tester; (d) INSTRON 1346 test system, AE system, and high-speed camera

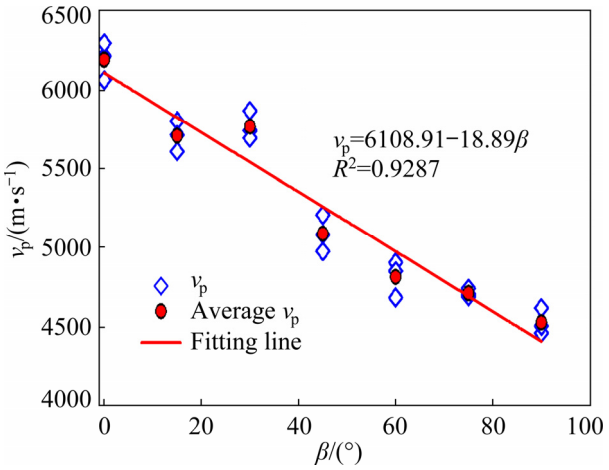

Fig. 4 Relationship between v_p and β

The reflection and refraction of ultrasonic waves at the bedding plane dissipated a part of the wave energy, resulting in the weakening of the wave propagation ability. When the bedding plane was parallel to the axial direction of the specimen (β=0°), the wave propagation direction was parallel to the bedding plane. Therefore, v_p of the specimen was the largest when β=0°. With an increase in β, the incident angle of the wave increased, the number of bedding planes that the wave needed to pass through during wave propagation increased, and the number of refractions and reflections between the bedding planes also increased. Therefore, the dissipated energy increased, which led to the weakening of the wave transmission ability and an increase in the transmission time, t, in the specimen. In addition, the height h of the phyllite specimens was the same (approximately 100 mm). According to the relationship among v_p, t, and h (v_p=h/t), v_p gradually decreased with increasing β, as shown in Fig. 4. When the bedding plane was perpendicular to the axial direction of the specimen (β=90°), the wave propagation direction was orthogonal to the bedding plane, and specular reflection occurred on the bedding plane. Thus, the wave propagation ability was the weakest, and the P-wave velocity was the smallest when β=90°.

3.2 Stress–strain curves

The stress–strain curves for different values of β (0°, 15°, 30°, 45°, 60°, 75°, and 90°) are shown in Fig. 5. These stress–strain curves can be divided into three types: rapid drop, sawtooth, and step drop. Their characteristics are as follows:

(1) Rapid-drop-type: In the initial stage, the curve was convex downward because of the compaction of the testing specimens. As the axial stress continued to increase, the stress–strain curve entered a linear growth stage, which was smooth and long; this stage corresponded to elastic deformation. There was a very small yield stage, and in some cases, no yield stage, before the peak stress was attained. When σ_1 was loaded to the peak stress, the specimen exhibited an overall instability and lost its bearing capacity; thus, the stress rapidly decreased to a low value, indicating that the specimen released a large amount of energy and experienced severe failure. This type of stress–strain curve was observed for Specimens 0-1, 0-2, 15-1, 30-1, 60-2, 60-3, 75-3, and 90-3.

(2) Sawtooth-type: In the initial stage, the curve was convex downward, and the specimen was in the compaction stage. For the same bedding angle, the curvature of the stress–strain curve during compaction was smaller than that of the rapid drop curve. With an increase in the axial stress, the stress–strain curve entered a linear growth stage and became smooth. A stress drop occurred before or after the peak stress, and the stress continued to increase near the peak stress, forming a sawtooth-type stress–strain curve, as observed for Specimens 0-3, 15-3, 30-2, 45-1, 45-2, and 90-2. Subsequently, the stress dropped rapidly, or in steps. The sawtooth-type stress–strain curve indicated that there was a weak bedding plane in the phyllite specimen. When the stress approached the peak, the weak bedding plane failed first, and the specimen still had bearing capacity; thus, it continued to bear the load. Consequently, the axial stress increased again, leading to the formation of a sawtooth-type stress–strain curve.

(3) Step-drop-type: The initial stage was similar to that of the above two types of stress–strain curves. After the specimen was loaded to the peak stress, stress dropped. During the post-peak stress drop, the stress was first reduced to a certain value, and then it remained relatively constant; however, the strain continued to increase, forming a post-peak stress plateau. Subsequently, stress further dropped. Thus, the stress was reduced to a lower value (approximately 0 MPa), and the curve resembled a step-drop-type curve. The stress–strain curves of this type were observed for Specimens 0-3, 15-2, 30-2, 30-3, 60-1, 75-1, 75-2, and 90-1.

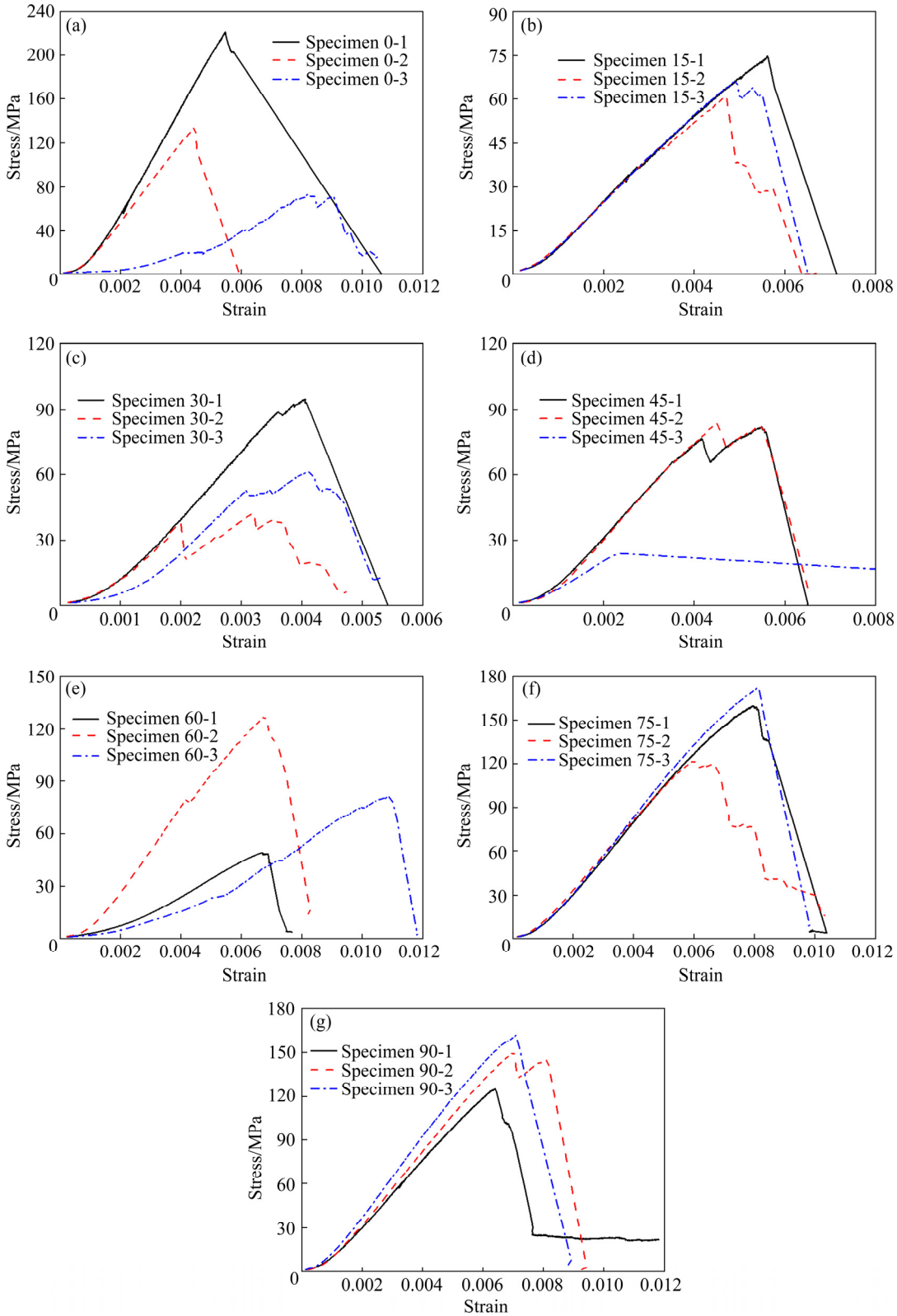

Fig. 5 Stress–strain curves: (a) β=0°; (b) β=15°; (c) β=30°; (d) β=45°; (e) β=60°; (f) β=75°; (g) β=90°

For the same bedding angle, the number of step drops was inversely proportional to the strength of the phyllite specimen. For example, the peak stress of Specimen 30-3 (step drop once) was higher than that of Specimen 30-2 (step drop twice; see Fig. 5(c)), and the peak stress of Specimen 75-1 (step drop twice) was higher than that of Specimen 75-2 (step drop three times; see Fig. 5(f)).

For the same bedding angle, the peak stress of the rapid-drop-type stress–strain curve was the highest, followed by that of the sawtooth-type curve, and that of the step-drop stress–strain curve was the lowest. Thus, the peak stress followed the order of Specimen 15-1 > Specimen 15-3 > Specimen 15-2 (Fig. 5(b)), and Specimen 90-3 > Specimen 90-2 > Specimen 90-1 (Fig. 5(g)). The stress–strain curves of phyllite specimens showed obvious anisotropy.

3.3 Mechanical properties of phyllite with different bedding angles

The test results of the mechanical parameters of the phyllite specimens under different bedding angles are listed in Table 1. The effects of β on the peak stress, peak strain, elastic modulus, Poisson's ratio, and brittleness index were investigated through uniaxial compression tests. The relationship between peak stress and β is shown in Fig. 6. The average peak stress decreased first, then increased, and finally decreased slightly with increasing β, showing a U-shaped trend. The maximum average peak stress of phyllite specimen was 151.48 MPa when β=75°, which was close to the average peak stresses at β=0° (143.02 MPa) and 90° (145.71 MPa). When β=45°, the average peak stress was the minimum, reaching 63.02 MPa, and was close to the average peak stress at β=15° (67.48 MPa) and 30° (65.91 MPa). Figure 6 shows that there were large differences among the values of the average peak stress attained under different bedding angles, i.e., the average peak stress at β=45° was 88.46 MPa, lower than that at β=75° (58.4% of average peak stress at β=75°). Therefore, a change in the bedding angle significantly affects the bearing capacity of phyllite.

Table 1 Mechanical parameters of phyllite specimens with different bedding angles

Specimen	Peak stress/MPa	σ_{ca}/ MPa	Peak strain	ε_a	Elastic modulus/GPa	E_a/ GPa	Poisson's ratio	μ_a	Brittleness index	B_a
0-1	221.50		0.0055		49.19		0.22		0.82	
0-2	134.41	143.02	0.0045	0.0061	35.95	33.28	0.24	0.21	0.84	0.75
0-3	73.17		0.0084		14.70		0.17		0.59	
15-1	74.79		0.0056		14.83		0.06		0.90	
15-2	60.89	67.48	0.0047	0.0051	15.16	15.05	0.21	0.19	0.85	0.88
15-3	66.75		0.0049		15.18		0.31		0.89	
30-1	94.54		0.0041		30.58		0.19		0.76	
30-2	41.91	65.91	0.0032	0.0038	24.00	26.96	0.26	0.24	0.55	0.62
30-3	61.28		0.0042		26.30		0.28		0.56	
45-1	81.74		0.0055		21.66		0.41		0.69	
45-2	83.36	63.02	0.0045	0.0041	23.27	19.12	0.17	0.23	0.80	0.77
45-3	23.96		0.0024		12.42		0.09		0.81	
60-1	49.09		0.0067		9.90		0.27		0.74	
60-2	127.77	85.93	0.0068	0.0068	24.50	15.14	0.20	0.22	0.77	0.73
60-3	80.91		0.0109		11.02		0.20		0.67	
75-1	159.71		0.0080		24.66		0.30		0.81	
75-2	122.88	151.48	0.0060	0.0074	23.89	24.83	0.25	0.25	0.86	0.83
75-3	171.86		0.0081		25.96		0.21		0.82	
90-1	125.13		0.0064		22.94		0.25		0.85	
90-2	150.16	145.71	0.0070	0.0068	25.30	25.24	0.18	0.18	0.85	0.84
90-3	161.84		0.0071		27.49		0.11		0.83	

σ_{ca} is the average peak stress (uniaxial compressive strength); ε_a is the average peak strain (the strain corresponding to the peak stress), E_a is the average elastic modulus, μ_a is the average Poisson's ratio, and B_a is the average brittleness index

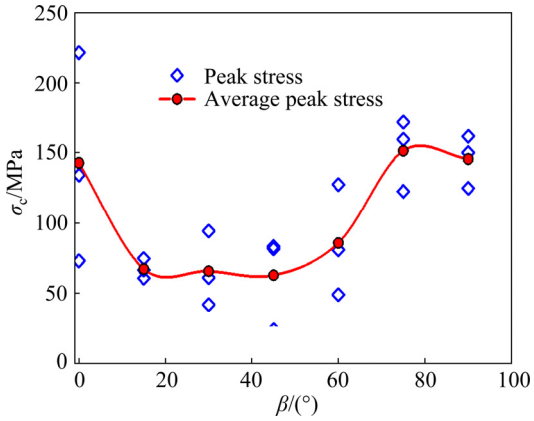

Fig. 6 Peak stress of phyllite with different bedding angles

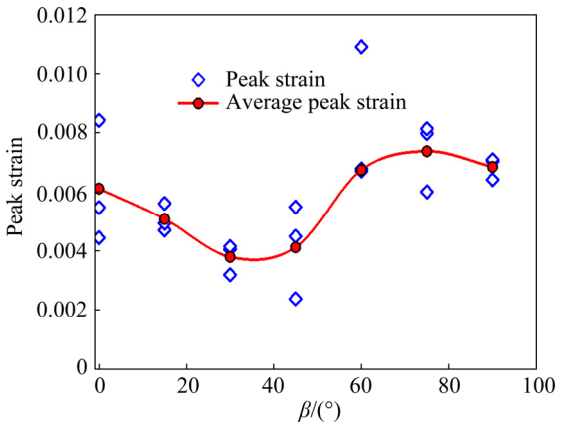

Fig. 7 Peak strain of phyllite with different bedding angles

The relationship between the peak strain and β is shown in Fig. 7. The peak strain of Specimen 60-3 is relatively discrete because it is too high. The peak strain of 0.0109 for Specimen 60-3 at failure was much higher than the peak strains of 0.0067 and 0.0068 for Specimens 60-1 and 60-2, respectively. The average peak strain of 0.0081 at β=60° was slightly higher than the average peak strain of 0.0074 at β=75°. In addition, when β=75°, the maximum difference among the peak strains of the three specimens (0.0080, 0.0060 and 0.0081) was 0.0021, which was only half the maximum difference of 0.0042 among the peak strains of the three specimens (0.0067, 0.0068, and 0.0109) when β=60°. Based on the spread of the test results attained at various bedding angles, the measurement result of the peak strain of Specimen 60-3 was considered an outlier that might have been caused by measurement error and was discarded. Thereafter, the variation trend of the peak strain with the bedding angle became U-shaped.

Figure 8 shows the relationship between the elastic modulus and β. The average elastic modulus decreased first, then increased, subsequently decreased, and finally increased with increasing β. The average elastic modulus at β=30° was higher than the average elastic modulus at β=15° and 45°. Although the average peak stress of the phyllite specimens was low at β=30°, the slope (elastic modulus) of the elastic phase of the specimen was large, which resulted in a high average elastic modulus of phyllite. The average Poisson's ratio of the phyllite specimens under different bedding angles was in the range of 0.18–0.25, as shown in Fig. 9.

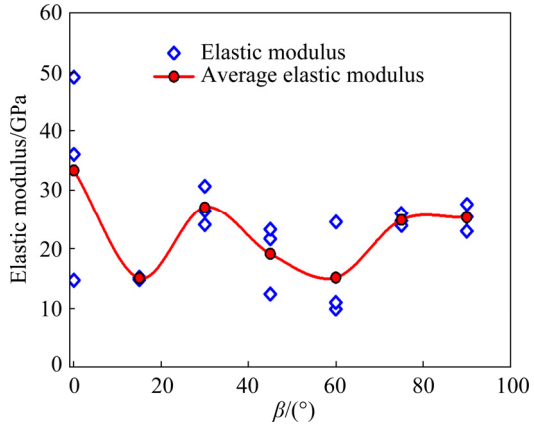

Fig. 8 Elastic modulus of phyllite with different bedding angles

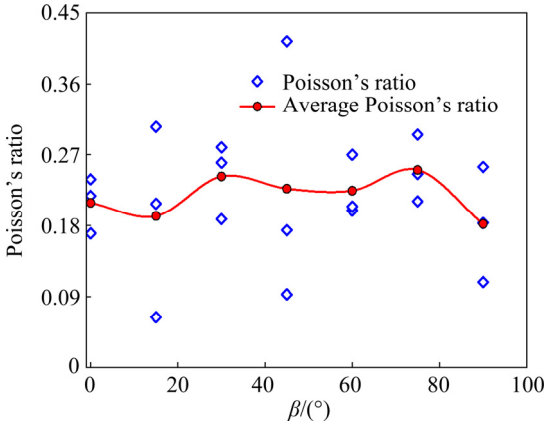

Fig. 9 Poisson's ratio of phyllite with different bedding angles

To investigate the brittleness response of phyllite specimens under different bedding angles, the brittleness index was calculated using the brittleness definition proposed by HUCKA and

DAS [25] (based on the ratio of reversible strain to the total strain at the peak stress point). The brittleness index of the phyllite specimens was relatively high, ranging from 0.62 to 0.88, as shown in Fig. 10.

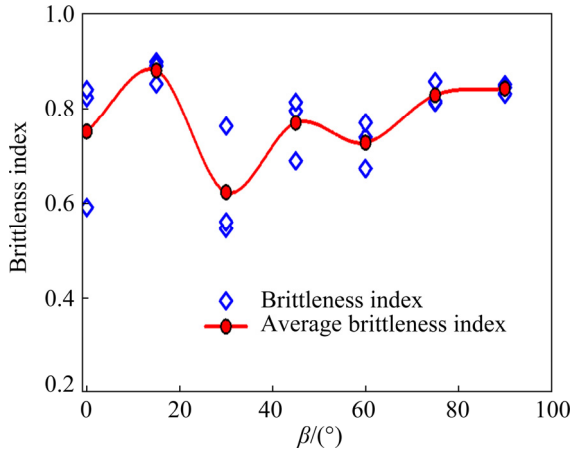

Fig. 10 Brittleness index of phyllite with different bedding angles

3.4 Failure mode

The failure photos of phyllite specimens under different bedding angles are shown in Fig. 11. The failure modes under different bedding angles were significantly different, leading to anisotropy. When β=0°, the failure mode was tensile splitting failure along the bedding plane, as shown in Fig. 11(a). Because the axial stress direction was parallel to the bedding plane in the uniaxial compression tests when the axial stress was slowly increased, the specimen was compressed without lateral restraint, and the hoop displacement gradually increased to cause transverse tensile stress. Under the action of the transverse tensile stress, tensile microcracks were generated gradually in the specimen. The cracks expanded along the direction of the weak bedding plane and finally penetrated the weak bedding plane to form macro cracks approximately parallel to the axial stress direction. The phyllite between the two bedding planes can be regarded as a compression strut structure. Therefore, the phyllite specimen split to form multiple independent compression struts that were almost parallel to the bedding plane. The parallel bedding plane experienced vertical tensile splitting failure. The peak stress of the rock specimen at β=0° was determined by the tensile strength of the weak bedding plane and the maximum compressive strength of the compression struts, whereas the residual strength was determined by the compressive strength of the compression struts.

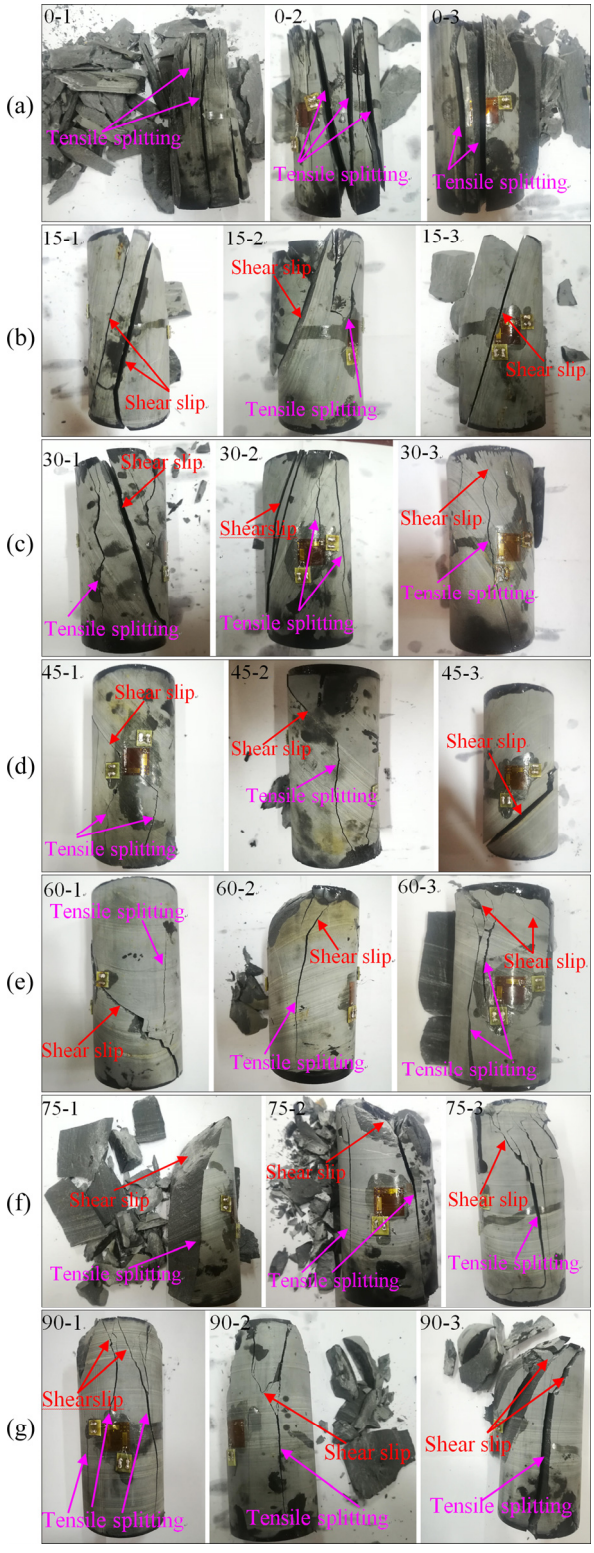

Fig. 11 Failure photos of phyllite specimens with different bedding angles: (a) β=0°; (b) β=15°; (c) β=30°; (d) β=45°; (e) β=60°; (f) β=75°; (g) β=90°

The failure mode was shear slip failure along

the bedding plane when β=15°, as shown in Fig. 11(b). This failure mode depended entirely on the cementation strength of the bedding planes. When β=30° and 45°, a mixed failure mode was observed, with shear slip failure along the weak bedding plane and tensile splitting failure across the bedding plane, as shown in Figs. 11(c) and 11(d), respectively. The specimen experienced shear slip failure along the weak bedding plane, and part of the macroscopic fracture surfaces crossed the bedding plane, as seen in Specimens 30-1, 30-2, 30-3, 45-1, and 45-2. For Specimen 45-3, shear slip failure occurred along the bedding plane. Under this failure mode, the peak stress of the phyllite specimen mainly depended on the degree of cementation of the weak bedding plane. Because the cementation strength of the phyllite bedding plane was low, the peak stress was also low.

When β=60° and 75°, the failure mode mainly manifested as a tensile splitting failure across the bedding plane, and shear failure occurred in the rock near the end surface of the specimen, as shown in Figs. 11(e) and 11(f). When β=90°, the failure mode was similar to that of the bedding angles of 60° and 75°, as shown in Fig. 11(g). Notably, shear failure did not occur along the bedding plane; rather, it occurred diagonally across the bedding plane. Because the axial stress was not strictly vertical to the bedding plane and there was end friction between the specimen and the loading block, shear stress was generated at the end of the specimen during the loading process, resulting in shear failure across the bedding plane at the end of the specimen. The end friction was reduced when the specimen was far from the loading block; the inside of the specimen was mainly subjected to tensile stress and experienced mainly tensile splitting failure. Under uniaxial compression without lateral restraint, the specimen could be freely deformed and peeled outward. The failure at β=90° was not controlled by the weak bedding plane but was determined by the tensile and shear strengths of the rock itself, as the cementation strength between the bedding planes was much lower than that of the phyllite rock particles. Thus, the peak stress of the phyllite specimen at β=90° was higher.

In summary, there were four failure modes of phyllite under different bedding angles: (1) tensile splitting failure along the bedding plane when β=0°, (2) shear slip failure along the bedding plane when β=15°, (3) a mixed failure mode of tensile splitting failure across the bedding plane and shear slip failure along the bedding plane when β=30° and 45°, and (4) tensile splitting failure across the bedding plane when β=60°, 75°, and 90°. When β was gradually increased from 0° to 90°, the failure mode of the phyllite specimens gradually transformed from tensile splitting failure along the bedding plane to shear slip failure along the weak bedding plane. Finally, the failure mode evolved into tensile splitting failure across the bedding plane in the parallel loading direction.

4 Discussion

4.1 AE characteristics

AE refers to the rapid release of the strain energy stored in a material, generating an elastic wave when the material is subjected to an external load, thereby producing sound [26,27]. Many scholars have investigated the characteristics of AE signals during rock failure and obtained useful results [28−34]. For example, ZHOU et al [28] and ZHANG et al [29] adopted the AE rate-process theory to analyze fracture-related AE event rate characteristics. WU et al [30] analyzed the relationships between the inflection points in the AE cumulative count curves and stress thresholds, and they proposed a new quantitative method for determining the crack damage stress of rock materials based on AE signal detection. NIU et al [31] investigated the classification of the fracture modes of rocks during the cracking process using uniaxial compression tests. These studies indicate that AE is an important method for monitoring specimen damage. AE parameters such as the AE counts and cumulative AE counts can accurately reflect the damage characteristics of rock during loading [35−37]. Figure 12 shows the profiles for the AE counts, cumulative AE counts, and stress of typical specimens with different bedding angles with respect to time. When β=30°, 45°, 60°, 75°, and 90°, some AE signals were generated during the initial loading stage, and the bedding plane of the specimen compacted. At β=0° and 15°, the compaction stage was not prominent, mainly because the bedding angle was low, and the

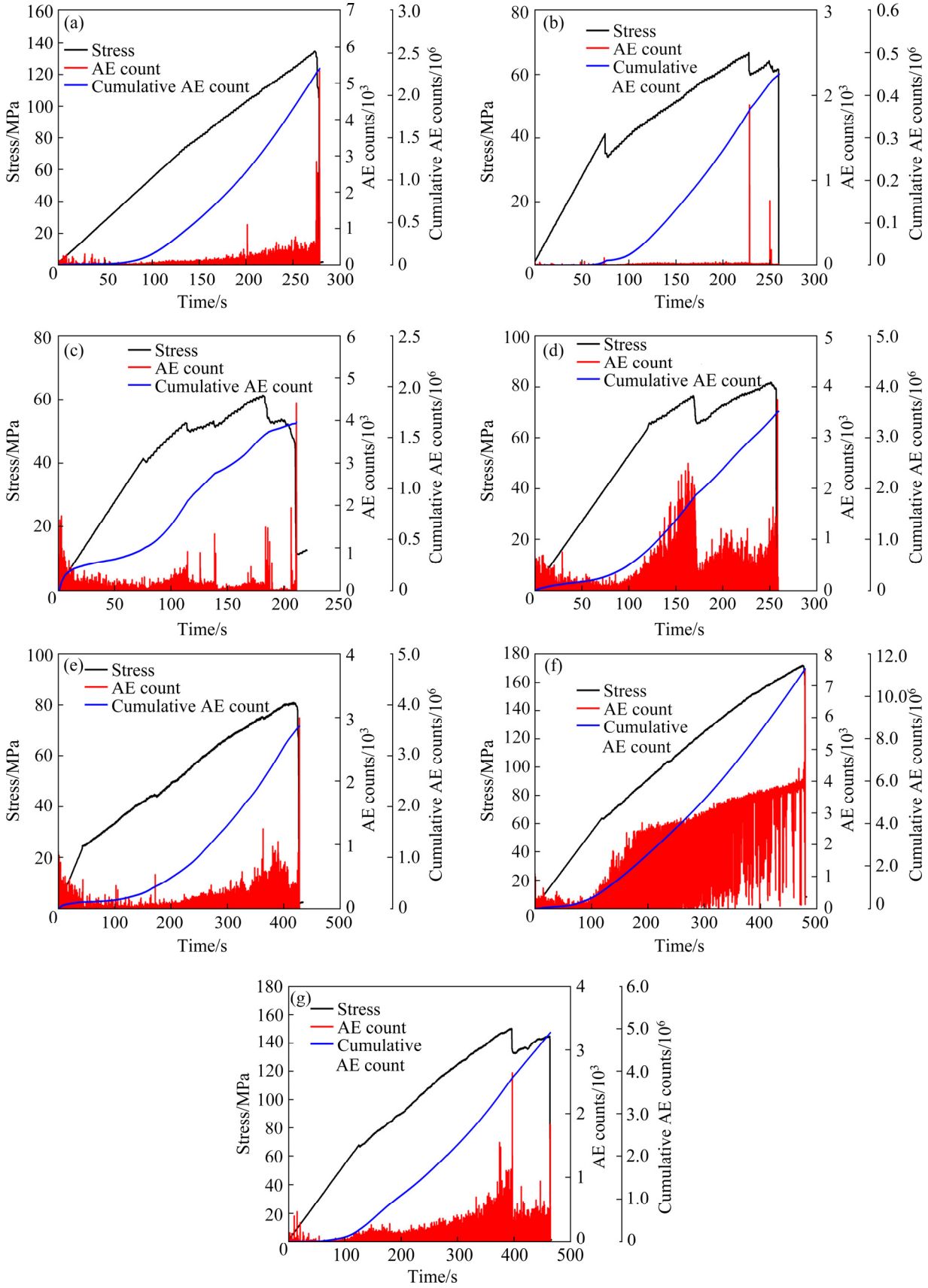

Fig. 12 Variation in AE counts and cumulative AE counts of typical phyllite specimens with different bedding angles: (a) β=0° (Specimen 0-2); (b) β=15° (Specimen 15-3); (c) β=30° (Specimen 30-3); (d) β=45° (Specimen 45-1); (e) β=60° (Specimen 60-3); (f) β=75° (Specimen 75-3); (g) β=90° (Specimen 90-2)

bedding plane was not prone to compaction. In the elastic stage, the signal intensity collected by the AE system was similar, and the AE signal was relatively smooth. When the axial stress was loaded to the plastic deformation stage, the specimen experienced rapid expansion, leading to the formation of cracks and causing a stress drop, which generated strong AE signals. The greater the stress dropped, the stronger the AE signal was. The cumulative AE counts for different bedding angles are shown in Fig. 13. The average cumulative AE counts showed an approximately U-shaped change trend as the bedding angle increased, which was consistent with the changing trend of the average peak stress. When β=0°, 60°, 75°, and 90°, the average cumulative AE counts were much higher than those when β=15°, 30°, and 45°. Therefore, the phyllite specimens produced a large number of AE events in the uniaxial compression tests at β=0°, 60°, 75°, and 90°, and the internal damage of the specimens was relatively severe.

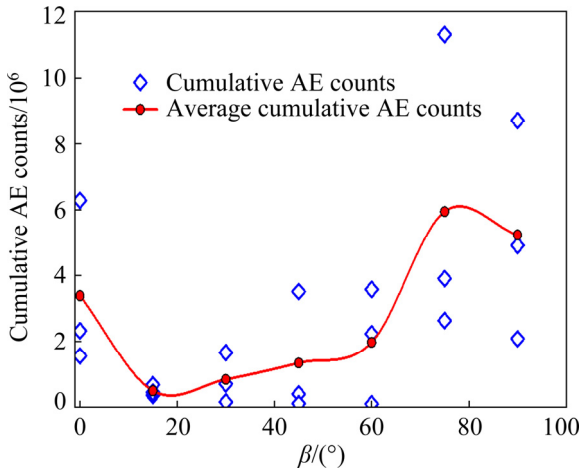

Fig. 13 Cumulative AE counts of phyllite specimens with different bedding angles

4.2 Failure process

The failure processes of typical phyllite specimens under different bedding angles are shown in Fig. 14. The initial failure time was set as the starting time (0 s). Figure 14(a) shows the failure process of Specimen 0-1 when β=0°. At 0.008 s, the specimen produced a longitudinal crack parallel to the bedding plane that was accompanied by particle ejection (see Fig. 14(a_2)). As shown in Fig. 14(a_3), a large number of rock fragments were rapidly ejected, accompanied by rock debris and rock powder. Many rock fragments flew out of the test bench, and some large rock slabs dropped on the test bench, as shown in Fig. 14(a_4). The failure process of Specimen 15-1 at β=15° is shown in Fig. 14(b). The specimen produced a crack parallel to the bedding plane (see Fig. 14(b_1)). Two penetrating cracks parallel to the bedding plane were generated at 0.008 s, and three rock blocks gradually separated and dropped, as shown in Figs. 14(b_2, b_3). A rock fragment flew out of the test bench, as shown in Fig. 14(b_4). The rockburst was relatively severe, demonstrating a strong shear slip rockburst. When β=30°, Specimen 30-2 exhibited slow shear slip failure and produced only one rock block, as shown in Figs. 14(c_1−c_3). A small rock fragment was produced during the sliding process, and all rock blocks were dropped on the test bench, as shown in Fig. 14(c_4). From the failure process, it was determined that the specimen underwent a slight shear slip failure, corresponding to a slight shear slip rockburst. At β=45°, Specimen 45-1 suffered a mixed failure of tensile splitting failure across the bedding plane and shear slip failure along the bedding plane. A rock block gradually flew out of the test bench, as shown in Figs. 14(d_1−d_4). The entire failure was relatively severe, demonstrating a strong rockburst. When β=60°, 75°, and 90°, the failure processes of Specimens 60-3, 75-1, and 90-2 were relatively similar, as shown in Figs. 14(e, f, g), respectively. These specimens produced approximately longitudinal tensile splitting cracks across the bedding plane, followed by the production of a large number of rock fragments accompanied by particle ejection. Many rock fragments flew out of the test bench. The failures were relatively severe, with the occurrence of strong strain rockbursts.

By comparing the failure processes of typical specimens under different bedding angles, when β=15°, 30°, and 45°, the failure of the specimens appeared as shear slip rockbursts, which produced large rock blocks. The failure range of the slip rockburst was relatively wide. When β=0°, 60°, 75°, and 90°, the failure of the specimens resulted in strain rockbursts. The range of strain rockbursts was relatively small. A large number of rock fragments and particles were generated during the rockburst. The specimens underwent extremely strong rockbursts, which were stronger than the shear slip rockbursts at β=15°, 30°, and 45°.

Fig. 14 Failure processes of typical phyllite specimens under different bedding angles: (a) β=0° (Specimen 0-1); (b) β=15° (Specimen 15-1); (c) β=30° (Specimen 30-2); (d) β=45° (Specimen 45-1); (e) β=60° (Specimen 60-3); (f) β=75° (Specimen 75-1); (g) β=90° (Specimen 90-2)

4.3 Rockburst proneness of phyllite with different bedding angles

Rockburst proneness is a type of reference index for investigating the impact proneness during rock fracture in uniaxial compression tests based on the mechanical properties of rock. Rockburst proneness is generally used to assess the severity of rockbursts in rock materials under certain conditions. Judging the rockburst proneness of rocks is an important aspect of rockburst disaster risk assessment in rock engineering. Many scholars have classified and analyzed rockburst proneness from the perspective of energy [38−42]. Phyllite exhibits anisotropic characteristics, and the bedding angle significantly influences the failure mode and peak stress. To investigate the rockburst proneness of phyllite specimens with different bedding angles, the potential energy of the elastic strain (PES, P) index [43,44] was used to determine rockburst proneness. In most cases, PES is expressed as follows:

$$P=\frac{\sigma_c^2}{2E} \tag{1}$$

where σ_c is the peak stress of the rock specimen in the uniaxial compression test, and E is elastic modulus of the loading curve. According to the criterion of the PES index, the rockburst proneness is classified into four categories: extremely strong rockburst proneness for P>200 kJ/m^3, strong rockburst proneness for 150 kJ/m^3 ≤ P ≤ 200 kJ/m^3, moderate rockburst proneness for 100 kJ/m^3 ≤ P < 150 kJ/m^3, and slight rockburst proneness for P < 100 kJ/m^3 [38]. The PES calculation results and rockburst proneness discrimination results are summarized in Table 2. The changing trend of the average PES with increasing bedding angle was similar to that of the peak stress, exhibiting a U-shape, as shown in Fig. 15. When β=0°, 60°, 75°, and 90°, the phyllite specimens exhibited extremely strong rockburst proneness. When β=15°, the average PES of the three phyllite specimens was

Table 2 PES calculation results and rockburst proneness discrimination results of phyllite specimens

Specimen	PES/(kJ·m^{-3})	Rockburst proneness discrimination result	Specimen	Average PES/(kJ·m^{-3})	Rockburst proneness discrimination result
0-1	499	Extremely strong	0-1		
0-2	251	Extremely strong	0-2	310	Extremely strong
0-3	182	Strong	0-3		
15-1	189	Strong	15-1		
15-2	122	Moderate	15-2	153	Strong
15-3	147	Moderate	15-3		
30-1	146	Moderate	30-1		
30-2	37	Slight	30-2	85	Slight
30-3	71	Slight	30-3		
45-1	154	Strong	45-1		
45-2	149	Moderate	45-2	109	Moderate
45-3	23	Slight	45-3		
60-1	122	Moderate	60-1		
60-2	333	Extremely strong	60-2	251	Extremely strong
60-3	297	Extremely strong	60-3		
75-1	517	Extremely strong	75-1		
75-2	316	Extremely strong	75-2	467	Extremely strong
75-3	569	Extremely strong	75-3		
90-1	341	Extremely strong	90-1		
90-2	446	Extremely strong	90-2	421	Extremely strong
90-3	476	Extremely strong	90-3		

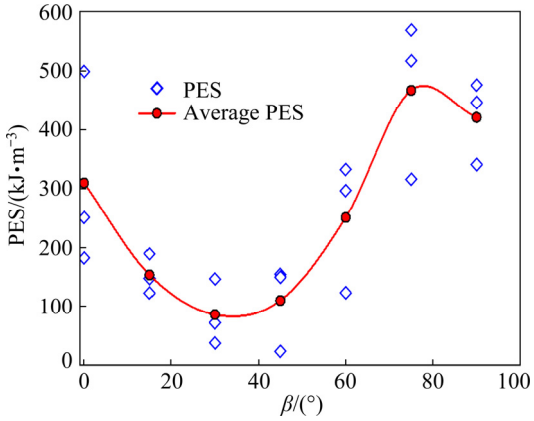

Fig. 15 PES of phyllite specimens with different bedding angles

153 kJ/m^3 and was between 150 kJ/m^3 and 200 kJ/m^3, indicating that the phyllite specimen had a strong rockburst proneness. When β=30°, the phyllite specimen exhibited a slight rockburst proneness. When β=45°, the phyllite specimen exhibited a moderate rockburst proneness. The discrimination results indicate that the bedding angle significantly influenced rockburst proneness, and the rockburst proneness of phyllite exhibited anisotropic characteristics.

4.4 Influence mechanism of bedding angle

The peak stress is closely related to the failure mode. For phyllite, there is a certain difference in the cementation strength between the bedding plane and rock particles, which may lead to the formation of a weak bedding plane in the specimen. The cementation strength among the bedding planes is much smaller than that among the rock particles; thus, the peak stress of the shear slip failure along the weak bedding plane is lower than that of the tensile splitting failure across the bedding plane. When β=0°, the failure mode was tensile splitting failure along the bedding plane, which was due to the instability failure of the compression struts. The peak stress depended on the independent compression struts, which reflected the ability of the bedding plane and compression strut structure of the phyllite specimen to resist shear and tensile failure. The strength of the phyllite structure was higher than that of the bedding plane, which led to higher peak stress at β=0°. When β=15°, 30°, and 45°, the failure mode was mainly shear slip failure along the weak bedding plane. The peak stress reflects the shear sliding resistance of the bedding plane, and the peak stress depends on the shear slip strength of the weak bedding plane. The peak stresses of the phyllite specimens were low because of the low shear slip strength of the weak bedding plane. When β=60°, 75°, and 90°, the failure mode was mainly tensile splitting failure across the bedding plane. The peak stress depended on the phyllite rock particles. The high compressive resistance of the phyllite rock particles gave the rock high peak stress. By combining the peak stress and failure mode of phyllite specimens under different bedding angles, the test results reveal that when β=0°, 60°, 75°, and 90°, the peak stress of the phyllite specimens was relatively high, which in turn caused high accumulation of energy inside the specimen. Extensive strain energy was released, and numerous particles were ejected when the specimens failed. The specimens exhibited extremely violent failure characteristics and extremely strong strain rockburst. Therefore, the specimens exhibited extremely strong rockburst proneness. In addition, because of the relatively high cumulative AE counts, the damage inside the specimen was severe, and the fragmentation degree after the experiment was relatively high. By contrast, when β=15°, 30°, and 45°, the peak stress of the phyllite specimens was relatively low, which in turn induced low energy accumulation inside the specimen. A shear slip rockburst occurred along the weak bedding plane, and the rockburst severity was relatively weak, leading to slight or moderate rockbursts. During the test, the low accumulative AE counts indicated that the internal damage of the specimens was low, resulting in the production of large rock blocks. Therefore, the transformation of the failure mode of phyllite is the primary reason for the U-shaped change trend of the peak stress, and the bedding angle has a controlling effect on the failure mode. The U-shaped change trend of the mechanical properties of bedding rocks explains the anisotropy of rockburst proneness and rockburst severity. The cumulative AE counts quantitatively characterize the degree of internal damage and rock fragmentation in the specimen.

5 Conclusions

(1) The P-wave velocity of the phyllite specimen gradually decreased with an increase in the bedding angle. The peak stress, peak strain, and

cumulative AE count showed U-shaped trend.

(2) There were four failure modes of phyllite specimens under different bedding angles: tensile splitting failure along the bedding plane (β=0°), shear slip failure along the bedding plane (β=15°), mixed failure mode of tensile splitting failure across the bedding plane and shear slip failure along the bedding plane (β=30° and 45°), and tensile splitting failure across the bedding plane (β=60°, 75°, and 90°). With an increase in β from 0° to 90°, the failure mode gradually transformed from tensile splitting failure along the bedding plane to shear slip failure along the weak bedding plane. Finally, the failure mode evolved into tensile splitting failure across the bedding plane in the parallel loading direction.

(3) The changing trend of the average PES with the bedding angle, which was U-shaped, was similar to that of the peak stress. When β=0°, 60°, 75°, and 90°, the phyllite specimens exhibited extremely strong rockburst proneness. When β=15°, the phyllite specimen exhibited a strong rockburst proneness. The phyllite specimen exhibited a slight rockburst proneness at β=30°. When β=45°, the phyllite specimen exhibited a moderate rockburst proneness.

(4) By comparing the failure process of phyllite specimens under different bedding angles, when β=15°, 30°, and 45°, shear slip rockbursts occurred in the specimens, and large rock blocks were produced. The failure range of the slip rockburst was relatively wide. When β=0°, 60°, 75°, and 90°, the failure of the specimens manifested as strain rockbursts. The failure range of the strain rockburst was relatively small. Several rock fragments and particles were generated during the strain rockburst, and the failure severity was stronger than that of the slip rockburst.

Acknowledgments

The authors are grateful for the financial supports from the National Natural Science Foundation of China (Nos. 51904335, 11972378, 41630642) and the Fundamental Research Funds for the Central Universities of Central South University, China (No. 2019zzts310).

References

[1] TIEN Y M, TSAO P F. Preparation and mechanical properties of artificial transversely isotropic rock [J]. International Journal of Rock Mechanics and Mining Sciences, 2000, 37: 1001−1012.

[2] XU Guo-wen, HE Chuan, SU Ang, CHEN Zi-quan. Experimental investigation of the anisotropic mechanical behavior of phyllite under triaxial compression [J]. International Journal of Rock Mechanics and Mining Sciences, 2018, 104: 100−112.

[3] HUANGFU Run, YAN Shun-xi, WANG Xiao-lei, JIANG Peng-cheng, ZHAN Si-bo. Study on infrared radiation characteristics of gneiss under uniaxial compression [J]. Journal of Mining and Strata Control Engineering, 2021, 3(1): 013011. (in Chinese)

[4] ZHANG Xue-ming, OU Xue-feng, GONG Feng-qiang, YANG Jun-sheng. Effects of bedding on the dynamic compressive properties of low anisotropy slate [J]. Rock Mechanics and Rock Engineering, 2019, 52: 981−990.

[5] GUO Yi-de, HUANG Lin-qi, LI Xi-bing, CHEN Jiang-zhan, SUN Jing-nan. Experimental investigation on the effects of thermal treatment on the physical and mechanical properties of shale [J]. Journal of Natural Gas Science and Engineering, 2020, 82: 103496.

[6] ALEJANO L, TABOADA J, GARCÍA-BASTANTE F, RODRIGUEZ P. Multi-approach backanalysis of a roof bed collapse in a mining room excavated in stratified rock [J]. International Journal of Rock Mechanics and Mining Sciences, 2008, 45: 899−913.

[7] DAMMYR Ø. Prediction of brittle failure for TBM tunnels in anisotropic rock: A case study from Northern Norway [J]. Rock Mechanics and Rock Engineering, 2016, 49: 2131−2153.

[8] LI Ang, SHAO Guo-jian, SU Jing-bo, SUN Yang, YU Tian-tang, SHI Hou-gai. Influence of heterogeneity on mechanical and acoustic emission behaviours of stratified rock specimens [J]. European Journal of Environmental and Civil Engineering, 2017, 22: 381−414.

[9] HENG Shuai, GUO Ying-tong, YANG Chun-he, DAEMEN J J K, LI Zhi. Experimental and theoretical study of the anisotropic properties of shale [J]. International Journal of Rock Mechanics and Mining Sciences, 2015, 74: 58−68.

[10] XU Feng, YANG Chun-he, GUO Yin-tong, WANG Lei, HOU Zhen-kun, LI Hao-ran, HU Xiao-ming, WANG Tong-tao. Effect of bedding planes on wave velocity and AE characteristics of the Longmaxi shale in China [J]. Arabian Journal of Geosciences, 2017, 10: 141−150.

[11] CHEN C, PAN E, AMADEI B. Determination of deformability and tensile strength of anisotropic rock using Brazilian tests [J]. International Journal of Rock Mechanics and Mining Sciences, 1998, 35: 43−61.

[12] DUAN K, KWOK C. Discrete element modeling of anisotropic rock under Brazilian test conditions [J]. International Journal of Rock Mechanics and Mining Sciences, 2015, 78: 46−56.

[13] HOEK E. Strength of jointed rock masses [J]. Geotechnique, 1983, 33(3): 187−223.

[14] SAROGLOU H, TSIAMBAOS G. A modified Hoek-Brown failure criterion for anisotropic intact rock [J]. International Journal of Rock Mechanics and Mining Sciences, 2008, 45: 223−234.

[15] ATTEWELL P, SANDFORD M. Intrinsic shear strength of a brittle, anisotropic rock—I: Experimental and mechanical interpretation [J]. International Journal of Rock Mechanics and Mining Sciences & Geomechanics Abstracts, 1974, 11: 423−430.

[16] RAMAMURTHY T, VENKATAPPA R G, SINGH J. Engineering behaviour of phyllites [J]. Engineering Geology, 1993, 33: 209−225.

[17] TIEN Y M, KUO M C. A failure criterion for transversely isotropic rocks [J]. International Journal of Rock Mechanics and Mining Sciences, 2001, 38: 399−412.

[18] FENG Guang-liang, FENG Xia-ting, CHEN Bing-rui, XIAO Ya-xun, ZHAO Zhou-neng. Effects of structural planes on the microseismicity associated with rockburst development processes in deep tunnels of the Jinping-II Hydropower Station, China [J]. Tunnelling and Underground Space Technology, 2019, 84: 273−280.

[19] SI Xue-feng, HUANG Lin-qi, LI Xi-bing, MA Chun-de, GONG Feng-qiang. Experimental investigation of spalling failure of D-shaped tunnel under three-dimensional high-stress conditions in hard rock [J]. Rock Mechanics and Rock Engineering, 2021, 54: 3017−3038.

[20] EVERITT R A, LAJTAI E Z. The influence of rock fabric on excavation damage in the Lac du Bonnett granite [J]. International Journal of Rock Mechanics and Mining Sciences, 2004, 41: 1277−1303.

[21] LI Xi-bing, GONG Feng-qiang, TAO Ming, DONG Long-jun, DU Kun, MA Chun-de, YIN Tu-bing. Failure mechanism and coupled static-dynamic loading theory in deep hard rock mining: A review [J]. Journal of Rock Mechanics and Geotechnical Engineering, 2017, 9(4): 767−782.

[22] LUO Yong, GONG Feng-qiang, LI Xi-bing, WANG Shan-yong. Experimental simulation investigation of influence of depth on spalling characteristics in circular hard rock tunnel [J]. Journal of Central South University, 2020, 27(3): 891−910.

[23] SI Xue-feng, GONG Feng-qiang. Strength-weakening effect and shear−tension failure mode transformation mechanism of rockburst for fine-grained granite under triaxial unloading compression [J]. International Journal of Rock Mechanics and Mining Sciences, 2020, 131: 104347.

[24] SI Xue-feng, HUANG Lin-qi, GONG Feng-qiang, LIU Xi-ling, LI Xi-bing. Experimental investigation on influence of loading rate on rockburst in deep circular tunnel under true-triaxial stress condition [J]. Journal of Central South University, 2020, 27(10): 2914−2929.

[25] HUCKA V, DAS B. Brittleness determination of rocks by different methods [J]. International Journal of Rock Mechanics and Mining Sciences & Geomechanics Abstracts, 1974, 11(10): 389−392.

[26] ZHOU Xiao-ping, PENG Sen-pin, ZHANG Jian-zhi, QIAN Qi-hu, LU Ri-chao. Predictive acoustical behavior of rockburst phenomena in Gaoligongshan tunnel, Dulong river highway, China [J]. Engineering Geology, 2018, 247: 117−128.

[27] LONG Yi, LIU Jian-po, LEI Gang, SI Ying-tao, ZHANG Chang-yin, WEI Deng-cheng, SHI Hong-xu. Progressive fracture processes around tunnel triggered by blast disturbances under biaxial compression with different lateral pressure coefficients [J]. Transactions of Nonferrous Metals Society of China, 2020, 30(9): 2518−2535.

[28] ZHOU Xiao-ping, ZHANG Jian-zhi, QIAN Qi-hu, NIU Yong. Experimental investigation of progressive cracking processes in granite under uniaxial loading using digital imaging and AE techniques [J]. Journal of Structural Geology, 2019, 126: 129−145.

[29] ZHANG Jian-zhi, ZHOU Xiao-ping, ZHOU Lun-shi, BERTO F. Progressive failure of brittle rocks with non-isometric flaws: Insights from acousto-optic-mechanical (AOM) data [J]. Fatigue & Fracture of Engineering Materials & Structures, 2019, 42(8): 1787−1802.

[30] WU Chen, GONG Feng-qiang, LUO Yong. A new quantitative method to identify the crack damage stress of rock using AE detection parameters [J]. Bulletin of Engineering Geology and the Environment, 2021, 80: 519−531.

[31] NIU Yong, ZHOU Xiao-ping, BERTO F. Evaluation of fracture mode classification in flawed red sandstone under uniaxial compression [J]. Theoretical and Applied Fracture Mechanics, 2020, 107: 102528.

[32] ZHOU Zi-long, ZHOU Jing, CAI Xin, RUI Yi-chao, CHEN Lian-jun, WANG Hai-quan. Acoustic emission source location considering refraction in layered media with cylindrical surface [J]. Transactions of Nonferrous Metals Society of China, 2020, 30(3): 789−799.

[33] LIU Xi-ling, LUO Ke-bing, LI Xi-bing, LI Qi-yue, WANG Wei-hua, GONG Feng-qiang. Cap rock blast caving of cavity under open pit bench [J]. Transactions of Nonferrous Metals Society of China, 2017, 27(3): 648−655.

[34] XU Shuai, LIU Jian-po, XU Shi-da, WEI Jiong, HUANG Wen-bo, DONG Long-bin. Experimental studies on pillar failure characteristics based on acoustic emission location technique [J]. Transactions of Nonferrous Metals Society of China, 2012, 22(11): 2792−2798.

[35] ZHANG Jian-zhi, ZHOU Xiao-ping. AE event rate characteristics of flawed granite: from damage stress to ultimate failure [J]. Geophysical Journal International, 2020, 222(2): 795−814.

[36] ZHANG Jian-zhi, ZHOU Xiao-ping. Forecasting catastrophic rupture in brittle rocks using Precursory AE Time Series [J]. Journal of Geophysical Research−Solid Earth, 2020, 125(8): e2019JB019276.

[37] ZHANG Bao-liang, SHEN Bao-tang, ZHANG Jin-hu, ZHANG Xin-guo. Experimental study of edge-opened cracks propagation in rock-like materials [J]. Journal of Mining and Strata Control Engineering, 2020, 2(3): 033035. (in Chinese)

[38] WANG J A, PARK H D. Comprehensive prediction of rockburst based on analysis of strain energy in rocks [J]. Tunnelling and Underground Space Technology, 2001, 16(1): 49−57.

[39] HE Ming-ming, ZHANG Zhi-qiang, ZHU Ji-wei, Li Ning, LI Guo-feng, CHEN Yun-sheng. Correlation between the rockburst proneness and friction characteristics of rock materials and a new method for rockburst proneness prediction: Field demonstration [J]. Journal of Petroleum Science and Engineering, 2021, 205: 108997.

[40] GONG Feng-qiang, WANG Yun-liang, LUO Song. Rockburst proneness criteria for rock materials: Review and new insights [J]. Journal of Central South University, 2020, 27(10): 2793−2821.
[41] LUO Song, GONG Feng-qiang. Linear energy storage and dissipation laws of rocks under preset angle shear conditions [J]. Rock Mechanics and Rock Engineering, 2020, 53: 3303−3323.
[42] LUO Song, GONG Feng-qiang. Linear energy storage and dissipation laws during rock fracture under three-point flexural loading [J]. Engineering Fracture Mechanics, 2020, 234: 107102.
[43] MUNOZ H, TAHERI A, CHANDA E K. Rock drilling performance evaluation by an energy dissipation based rock brittleness index [J]. Rock Mechanics and Rock Engineering, 2016, 49(8): 3343−3355.
[44] GONG Feng-qiang, YAN Jing-yi, LUO Song, LI Xi-bing. Investigation on the linear energy storage and dissipation laws of rock materials under uniaxial compression [J]. Rock Mechanics and Rock Engineering, 2019, 52(11): 4237–4255.

单轴压缩下千枚岩的力学特性和岩爆倾向性

司雪峰[1]，黄麟淇[1]，李夕兵[1]，宫凤强[2]，刘希灵[1]

1. 中南大学 资源与安全工程学院，长沙 410083；
2. 东南大学 土木工程学院，南京 211189

摘 要：为了研究层理角度β对力学特性和岩爆倾向性的影响，对不同层理角度下的圆柱体千枚岩试样进行单轴压缩试验。结果表明，峰值应力、峰值应变、累计声发射计数和弹性应变势能均呈 U 形变化趋势。随着β从 0°增大到 90°，破坏模式从沿着层理面的拉伸劈裂破坏转变为沿着弱层理面的剪切滑移破坏；最终，破坏模式演变为穿越层理面的拉伸劈裂破坏。当β=15°、30°和 45°时，千枚岩试样分别表现出强烈、轻微和中等岩爆倾向性，并且分别发生强烈、轻微和中等的剪切滑移型岩爆。当β=0°、60°、75°和 90°时，千枚岩试样具有极强的岩爆倾向性，并且发生极强的应变型岩爆。

关键词：千枚岩；层理角度；力学特性；破坏模式转化；岩爆倾向性

(Edited by Bing YANG)